# ACCELERATING AGING FAILURES IN MEMS DEVICES

Danelle M. Tanner, Jeremy A. Walraven, Michael T. Dugger, Ted B. Parson,
Sam A. Candelaria, Mark W. Jenkins, Alex D. Corwin, James A. Ohlhausen, and Elizabeth M. Huffman
Sandia National Laboratories
PO Box 5800, MS 1310, Albuquerque, NM 87185-1310
505-844-8973; e-mail: tannerdm@sandia.gov

## ABSTRACT

The feasibility of using temperature and humidity to age vapor-deposited SAM-coated electrostatic-actuated MEMS devices with contacting surfaces was determined. Failures were dependent on both temperature and humidity. The trend indicated longer life at both lower temperatures and lower humidity levels. Using cantilever beams, measurements reveal degradation of the VSAM surface coating when stressed at 300°C with controlled humidity environments of 500 and 2000 ppmv. In particular, we have seen the surface adhesion change for these beams stressed at 300°C for time intervals of 10, 24, 50, 100, and 200 hours. However, there is no measurable change after 2 hours. The higher humidity case promotes the same surface adhesion change in a factor of ten less time. The complex MEMS devices tested followed the same trends as the beam test structures. We definitely observe a failure of the MEMS devices due to the environment with most failures occurring at 300°C and some failures at 200°C. These failures are due to an adhesion site in the hub of the load gear where the typical gap is 0.3 μm.

[*Keywords:* MEMS, MEMS dormant storage, MEMS accelerated life tests, VSAM degradation]

## INTRODUCTION

Many MEMS devices have applications where they sit in storage for a long period of time and then must operate when requested. If the device is complex with surfaces in contact, surface interactions over time can determine whether a device functions or not.

A critical factor in the long term reliability of surfaces in contact during storage is the stability of monolayer coupling agents applied during processing to reduce adhesion. These coatings are popular processing aides because they can be applied at the back end of the manufacturing line, thus having no impact on the fabrication process. The coatings are typically one molecule thick, and as such do not modify the stress state of the polycrystalline silicon layers. The adsorbed films are also self-limiting in thickness, and can penetrate through the liquid or vapor phase to coat deeply hidden interfaces.

Srinivasan et al. exposed alkylsilane films (octadecyltrichlorosilane, $CH_3(CH_2)_{17}SiCl_3$ and perfluorodecyltrichlorosilane, $CF_3(CF_2)_7(CH_2)_2SiCl_3$) to water vapor at elevated temperatures and showed that reaction with water can cause treated silicon surfaces to become less hydrophobic. [1] Results showed that while the fluorocarbon silane maintained a water contact angle above 100 degrees in air up to 400ºC, the hydrocarbon film exhibited a water contact angle below 90 degrees after heating to 200ºC in air. When heated in nitrogen both films exhibited hydrophobic surfaces after heating to 500ºC for 5 minutes, above which the water contact angle decreased rapidly due to thermal decomposition of the monolayers. Kluth et al. performed thermal desorption studies with isotopically tagged alkylsilanes, and found that C-C bond cleavage in a hydrocarbon film begins at about 470ºC in vacuum, and a similar mechanism is expected for the fluorocarbon molecules. [2] The increased stability of fluorocarbon films in air is believed to be due to higher activation energy for hydrolysis caused by the fluorine atoms that are more difficult to polarize than hydrogen atoms. In the first examination of silane reactions with water at concentrations below 5000 ppm, Dugger et.al demonstrated similar stability of perfluorodecyltrichlorosilane monolayers after exposure to 300ºC and 4261 ppm water vapor, while under the same conditions octadecyltrichlorosilane monolayers were found to degrade significantly. [3] However, fluorocarbon films were found to be more susceptible to degradation after radiation exposure than hydrocarbon films. Thus, for short-term exposures at least, fluorinated silane coupling agents appear to be stable on silicon in environments containing water vapor at temperatures up to 400ºC. In order to insure reliable performance after long term storage of devices having surfaces in contact, however, monolayer degradation in package environments containing low levels of water vapor must be examined, and the impact of changes in surface composition on device functionality determined.

We have two main objectives for this work. The first is to determine if failures in complex MEMS devices can be accelerated using high temperatures and controlled humidity environments. The second objective is to relate these failures to measurable changes in contacting surfaces using test structures and surface analysis techniques.

## EXPERIMENTAL PROCEDURE

The MEMS devices were fabricated in Sandia National Laboratories SUMMiT™ process. Each die was attached to a 24-pin DIP ceramic package without a lid for environmental testing. In addition to functioning devices, we have diagnostic test structures on each die to enable surface adhesion measurements. The die in this test had a coating deposition scheme termed VSAM (vapor-deposited self-assembled monolayer) that employed supercritical $CO_2$ drying followed by the chemical vapor deposition of a fluorinated-amino silane precursor. Specifically, for these tests, we used FOTAS, $C_8F_{13}H_4Si(CH_3CH_3N)_3$ which has been shown to achieve repeatable yield of complex devices through typical packaging processes. [4]

Controlled environment tubes were designed and fabricated to enable testing in standard ovens. The tubes were constructed from stainless steel in order to facilitate cleaning and minimize sources of contamination. All tubes, frame structures, and screws were subjected to a chemical wash to remove any organic contamination prior to package insertion and exposure to temperature. Each tube has the capability to hold 20 packages. The packages were mounted in a grounded frame as shown in Figure 1. The frame, packages, and tube were placed in a controlled environment glove box, containing the test environment of interest, for a 24-hour period to reach equilibrium. Then the frame was inserted into the tube and sealed using the copper gasket and end plate. Care was taken to insure oxygen levels of < 10 ppmv.

Nitrogen was chosen as a typical package atmosphere. We have chosen accelerated stress temperature levels of 200°C and 300°C which are higher than the standard product operating range of -55°C to +125°C. The two humidity levels of 500 and 2000 ppmv $H_2O$ chosen are lower than the military-standard of 5000 ppmv (15.8%

RH at 25 °C) because of the known sensitivity of MEMS devices to humidity. [5, 6] Additionally, hermetic packaging processes exist to easily reach the 5000 ppmv $H_2O$ level. We want to determine if there is a susceptibility to lower levels of moisture.

For each temperature and humidity level, we tested for three time intervals. We used roughly 30 packages for each test to insure a good statistical sample and included a bare silicon die package to perform surface analysis after the test. A control set of packages was also stored in a dry nitrogen environment throughout the length of the experiments. After the test for the defined time interval, the packages were removed from the environmental tubes and devices were checked for functionality in ambient air. Failed devices were analyzed and functioning devices were censored from further testing. Each time interval has a different set of devices.

*TRA Device*

The MEMS device chosen for aging was a Torsional Ratcheting Actuator (TRA) which uses rotational comb drives for electrostatic operation. [7] A large circular frame ties the movable banks of combs together. A SEM image of the fabricated device is shown in Figure 2. Four cantilever beams support this frame in its center and act as the frame's spring return. These four beams are stiff to any lateral motion of the frame but compliant to rotation. There are three ratchet pawls and three anti-reverse pawls located symmetrically around the ring gear. Four guides are used to maintain alignment of the ring gear, constraining motion along the x, y, and z planes. The TRA rotates the load gear which contains a toggle beam between the gear teeth that applies a tangential resisting force of 24 μN.

For operation, a periodic voltage is applied between the stationary and moving combs. As the voltage increases, the torsion frame rotates counter-clockwise about its springs in response to the electrostatic attraction. As the frame begins to rotate, the ratchet pawls engage the ring gear and cause it to rotate also (Figure 3). As the gear is rotating, the anti-reverse pawls are forced out of their engagement with the ratchet teeth. Once the ring gear has moved sufficiently, the anti-reverse pawls engage the next tooth. When the voltage is removed, the central torsion springs force the frame to return to its rest position. As the frame is returning, the ratchet pawls attempt to drag the ring gear in the reverse direction via friction of the ratchet pawls with the ring gear. Because the anti-reverse mechanisms have engaged, the ratchet pawls are forced to skip over the tooth and finally engage the next tooth. At this point, the frame has returned to its initial position, and the cycle can be repeated. A pulsed 50 V saw-tooth signal was used for actuation.

Susceptible regions of the TRA that are in intimate contact are the hub region of the load gear, the toggle beam on the load gear, the dimples that support the ring gear, and any interaction points of the

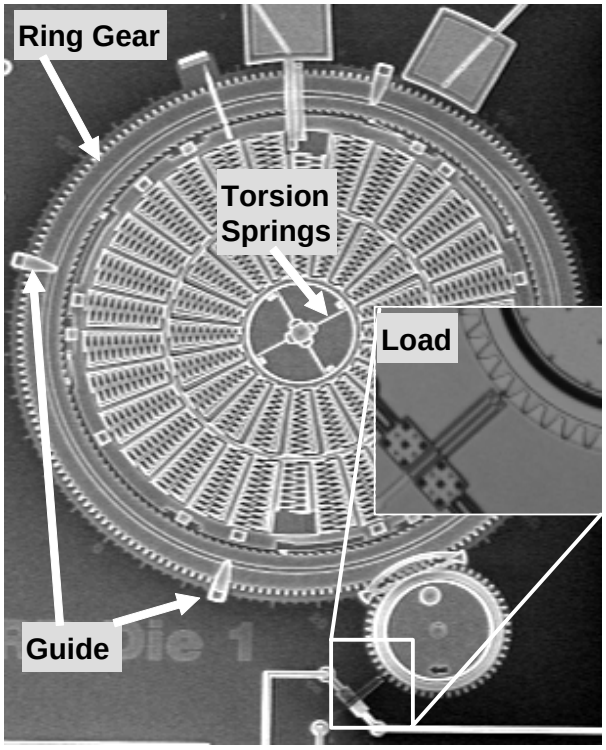


Figure 2. This SEM image of the fabricated torsional ratcheting actuator shows the guide and ring mechanisms. The inset shows an enlarged view of the load gear and beam.

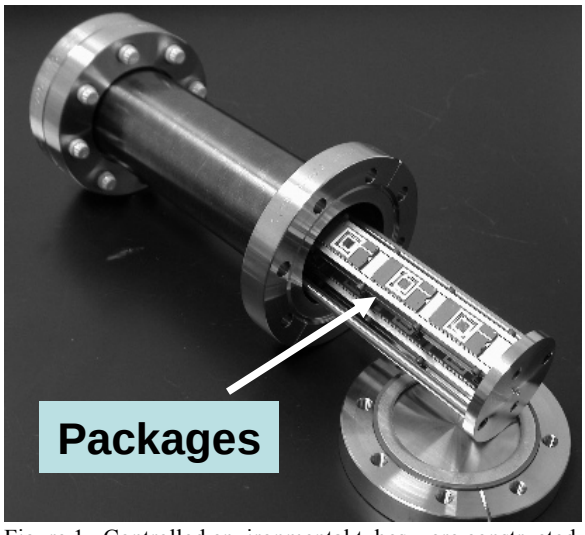


Figure 1. Controlled environmental tubes were constructed to define the test environment. The package placement inside the tubes is shown here.

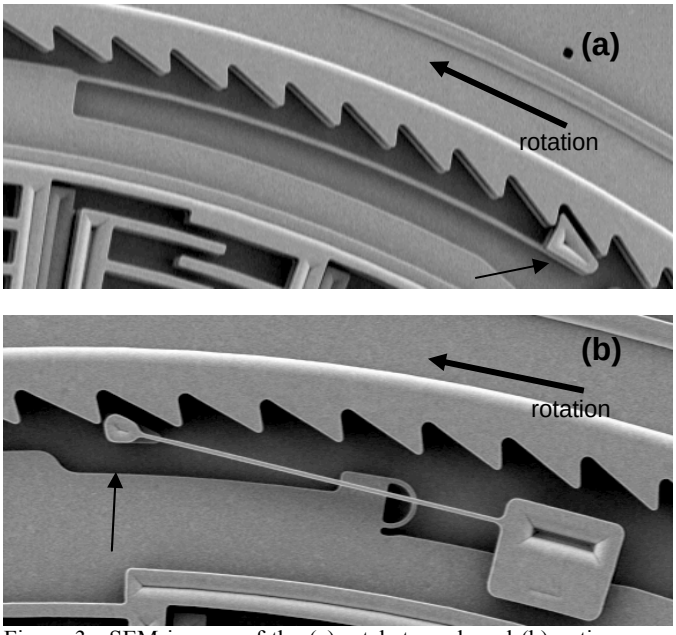


Figure 3. SEM images of the (a) ratchet pawl, and (b) anti-reverse pawl. The rotation direction of the ring gear is shown by the arrow.

meshing teeth or ratchet pawls. The gap in the hub was nominally 0.3 μm and was fabricated using the same process described in earlier work investigating wear of contacting surfaces. [8] In that work, we observed adhesion in the contacting surfaces, but only after over 100,000 cycles and using a higher force than applied here. These devices are only operated for tens of cycles to check functionality.

### *Cantilever Beam Array*

Each die has in addition to the MEMS device, a cantilever beam array to allow surface adhesion characterization. A technique was developed by de Boer and Michalske to measure surface adhesion by using cantilever beam arrays. [9] The procedure uses interferometry to measure s-shaped deflections in cantilever beams when they are adhered to the substrate. As shown in Figure 4, a beam is pulled into contact with the substrate by applying 90V to an actuation pad near the beam support. When the voltage is released, the restoring force of the beams and the adhesion of the surface come to equilibrium. The crack length, s, the length from the support post to the point the beam is adhered, was extracted from the measured deflection for each cantilever beam. The adhesion energy depends on the inverse of this parameter to the fourth power. The equation used was

$$\Gamma = \frac{3Et^3h^2}{2s^4} \qquad (1)$$

where the standard value for E, Young's modulus, was 165 GPa, the thickness, t, was 2.5 μm, and the gap, h, was 1.8 μm.

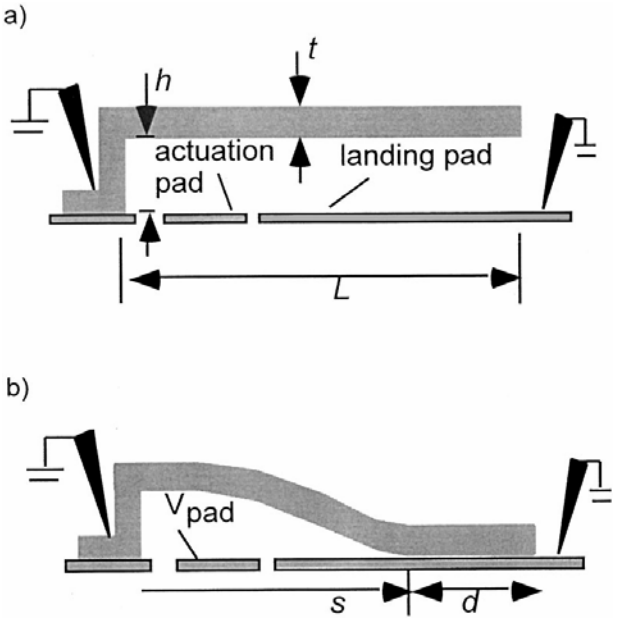


Figure 4. This schematic illustration of the approach for measuring the surface adhesion between silicon surfaces shows a) the basic free-standing beam with appropriate parameters and b) the adhered beam after it was pulled into contact by applying and then removing a voltage with the voltage, $V_{pad}$.

## RESULTS AND DISCUSSION

### *Surface Adhesion*

We have characterized the adhesion energy of the surfaces of control die and test specimens using cantilever beam arrays. In early experiments, we simply compared control die to post-test die. However, to discern changes more accurately, for later experiments, we decided to measure the same beams both pre-test and post-test. For example, in the 200-hour exposure, we used an actuation voltage to force the beams into contact with the substrate (zip beams), released the voltage, and measured adhesion. These beams were then exposed to the environments in their 'zipped' equilibrium state. The advantage of this method is that we then investigate the very same beams after test so that we have a clear before and after description of the surface adhesion.

A comparison is shown in Figure 5 of a control die which is kept in a dry nitrogen environment with no temperature stress and a die that was tested at 300°C for 50 hours with a humidity level of 572 ppmv. The fringes indicate deflections of the beam; sections of no fringes indicated adhered beams. The measured crack length of 870 μm for this particular control was used to calculate a surface adhesion of 14 μJ/m$^2$ using equation 1. The test specimen had a crack length of 470 μm which equates to a surface adhesion of about 260 μJ/m$^2$. Control beam arrays that were stored in a dry-nitrogen environment during the test showed virtually no change in the adhesion energy over longer time intervals.

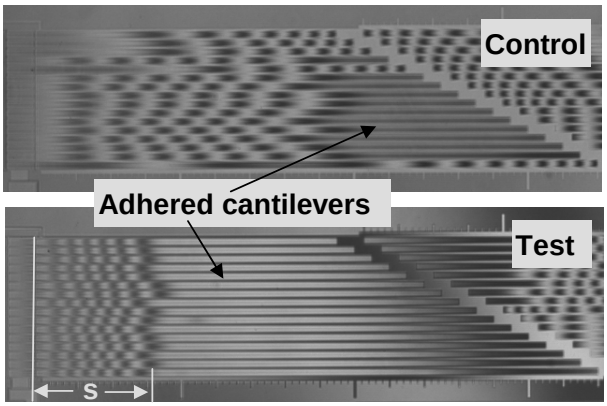


Figure 5. These interferograms of cantilever beam arrays on the different dice show the beams that are adhered to the substrate. The crack length, s, shown on the test beams was extracted from the measured deflection for each beam.

Analyzing the beam arrays from the various experiments showed the greatest effect in surface adhesion change in the 300°C experiments. There was no measurable change in surface adhesion for the 200°C experiments and the two-hour, 300°C experiment. Figure 6 shows the data obtained in the low humidity, 300°C case. Each data point represents a single cantilever beam. The measured value of crack length for the control or pre-test case was plotted for each time interval. These crack length values were averaged with outliers eliminated to represent a single value for that condition. The standard deviation of the crack lengths was determined as a measure of the spread in the data. The variation in the measurement in crack lengths could be due to a non-uniform distribution of the VSAM coating. The gap under the cantilever is 1.8 μm which should allow good coverage.

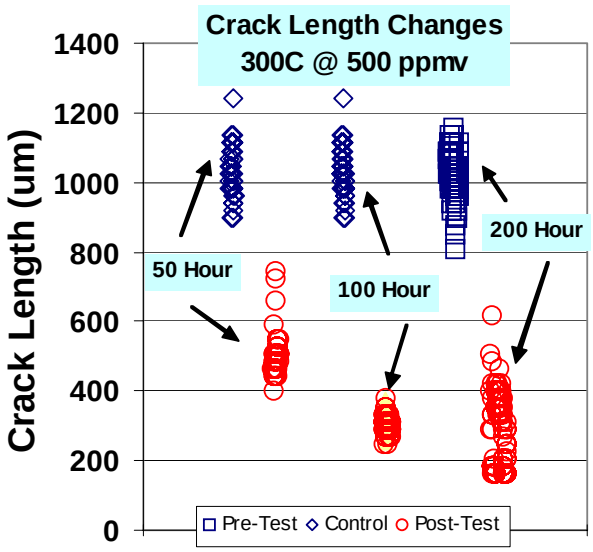


Figure 6. This scatter plot of cantilever beam crack length measurements shows differences between control and post-test devices for the time intervals indicated. For the 200 hour test, the pre-test measurements were on identical beams as the post-test measurement.

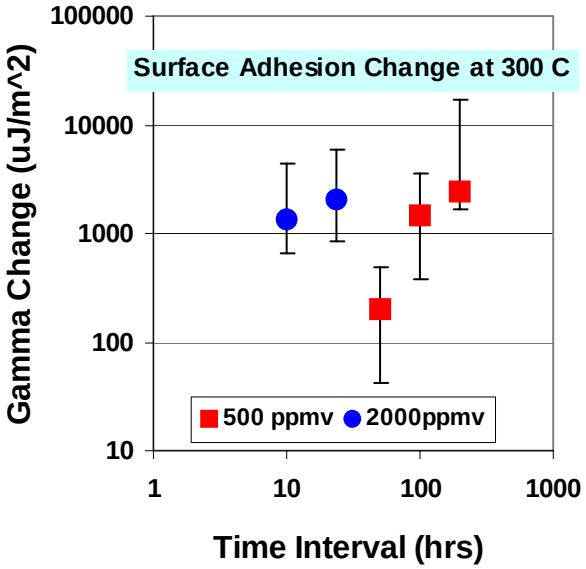


Figure 7. The change in surface adhesion as a result of environment is shown here. The data show both a humidity and time dependence. Shorter time intervals at higher humidity produce the same surface degradation as longer times at lower humidity.

The large variability in the crack length measurement produces an even larger spread in surface adhesion. The standard deviation of each group was used to calculate a lower and upper error on the surface adhesion. Table 3 shows analyzed crack length data, ***s***, and associated calculated values of surface adhesion energy.

Table 3. Analyzed crack length data, ***s***, for 300 degree C stress

| Humidity (ppmv) | Time Interval (hours) | Pre-Test ***s*** (μm) | Pre-Test ***s*** St. Dev. (μm) | Post-Test ***s*** (μm) | Post-Test ***s*** St. Dev. (μm) | Gamma Diff ($\mu J/m^2$) |
|---|---|---|---|---|---|---|
| 2280 | 2 | 1058 | 58 | 1052 | 58 | 0.2 |
| 2150 | 10 | 875 | 58 | 310 | 58 | 1336 |
| 2150 | 24 | 875 | 58 | 279 | 42 | 2042 |
| 572 | 50 | 1025 | 65 | 491 | 36 | 204 |
| 488 | 100 | 1025 | 65 | 304 | 36 | 1462 |
| 508 | 200 | 1030 | 24 | 269 | 96 | 2399 |

Of particular concern is the change in the surface adhesion due to the environment and how that relates to device failures. Figure 7 shows the change in surface adhesion of the 300°C cantilevers as a function of stress time interval. The error bars represent a ±1 standard deviation in the measured crack lengths. The inverse fourth-power dependence on crack length gave rise to the non-symmetric range indicated in the figure. The 2-hour time interval was not included. Shorter time intervals at higher humidity produce the same surface degradation as longer times at lower humidity.

### *ToF-SIMS Surface Analysis*

For each set of experiments, we add monitor bare silicon die at all stages of preparation and test. Four Si die go through the release, dry, and coat (RDC) process. Of those four, one is held in a gel pack in a dry nitrogen environment, and the other three are packaged with the test specimens. One packaged Si die remained as a control in a dry nitrogen environment and the other two were put on test.

Data were acquired using a Physical Electronics TRIFT I Time-of-Flight Secondary Ion Mass Spectrometer (ToF-SIMS) system. Spectral images were acquired in positive secondary ion mode using a 25 kV, 200 nm-sized, 600 pA, $^{69}Ga$ static beam rastered over a 65 x 65 $\mu m^2$ analysis region. Raw files were stored during each 5 minute acquisition with no charge compensation methods employed. The data contained in each raw file were binned to 256x256 pixel images with spectra ranging from 0-400 amu at 1-amu bins. The spectral images were concatenated together to form a spectral image montage. The resulting spectral image montage was processed using Sandia National Laboratories' multivariate analysis program, AXSIA (Automated eXpert Spectral Image Analysis). [10] Using this technique, we observed a degration in the VSAM coating as shown in Figure 8.

Similar signatures were obtained for other chemicals. We observed a flourinated Si substrate with unknown hydrocarbons after the packaging process. The hydrocarbons vanish with 50 hour and 100 hour tests, but we observe an increase in silicone and the fluorinated Si substrate. The silicone contamination was likely a contamination from the gel packs used for storage before and after tests.

### *TRA Device*

The major challenge in these experiments was due to the excessive amount of handling of these unprotected die. As a result, it was necessary to eliminate devices due to breakage, electrostatic discharge effects, and particle contamination. As mentioned earlier in the procedure, all packages are removed from the environment tubes and tested for functionality in an ambient air environment. The

raw data from the completed series of experiments is shown in Table 1. The censored data column was the number of functioning devices removed from the test at the end of that time interval. The removal of functioning devices necessitated use of the Kaplan-Meier technique for multiply censored interval data. [11]

Table 1. TRA Failure Data.

| Temperature (degree C) | Actual Humidity (ppmv) | Time Interval (hours) | Number Failed | Number Censored | Total on Test |
|---|---|---|---|---|---|
| 300 | 2280 | 2 | 0 | 24 | 24 |
| 300 | 2150 | 10 | 7 | 3 | 10 |
| 300 | 2150 | 24 | 3 | 6 | 9 |
| 200 | 2050 | 518 | 2 | 13 | 15 |
| 200 | 1990 | 1000 | 2 | 15 | 17 |
| 300 | 570 | 50 | 4 | 20 | 24 |
| 300 | 490 | 100 | 3 | 20 | 23 |
| 300 | 510 | 200 | 6 | 7 | 13 |
| 200 | 480 | 500 | 1 | 23 | 24 |
| 200 | 470 | 1000 | 1 | 26 | 27 |

Failure data from the upper temperature of 300°C and the two humidity levels is shown in Figure 9. We observed a mean time to failure of 25 hours for the 300°C, 2000 ppmv tests and a mean time to failure of 256 hours for the 300°C, 500 ppmv tests. This indicates a strong link to moisture content.

Each lognormal distribution can be described by the median number of cycles to failure and a slope parameter, σ. The median number of cycles to failure is simply the intersection of the data fit line and the 50% cumulative failed. The slope parameter is the slope of the fit line on a log scale. This slope of the line fit was used to estimate a 90% confidence interval for the median times to failure using the equation:

$$\pm CI = t_{50} 10^{\pm 0.1\sigma/\sqrt{N}} \qquad (2)$$

The same technique was used to analyze all of the time interval data from other experiments. The 2000-hour experiments for the 200°C are still in process, which adds uncertainty to the lognormal fits to the data. The predicted median times to failure and averaged humidity levels are shown in Table 2.

Table 2. Analyzed data from all experiments.

| Temperature (degree C) | Average Humidity (ppmv) | $t_{50}$ (hours) | σ | -CI (hours) | +CI (hours) |
|---|---|---|---|---|---|
| 200 | 2020 | 2600 | 0.9 | 1310 | 5130 |
| 300 | 2190 | 26 | 1.0 | 14 | 48 |
| 200 | 477 | 9200 | 0.9 | 4670 | 17900 |
| 300 | 522 | 312 | 1.0 | 196 | 496 |

The 200°C, low humidity data had time intervals with only 1 failure. Care must be taken in the interpretation of those failures as accidental inclusion of a handling failure would skew the results. We had one case where we observed a failure in the controls due to handling. Figure 10 shows the data from all experiments. The trend to longer life at both lower temperature and lower humidity is apparent. This data shows the same trend as the surface adhesion data shown in Figure 7 indicating that surface adhesion is a candidate failure mode. We used this data only to observe trends; there is not enough solid data or understanding of the failure mechanism to begin predictive model development.

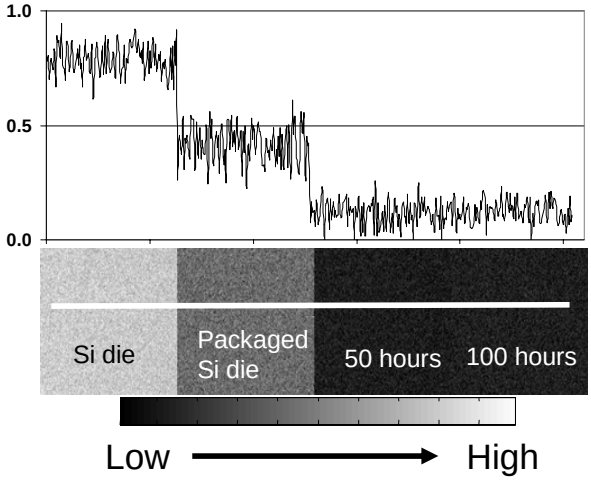


Figure 8. Each block represents the 65 x 65 µm scan sample of the Si die under different conditions. A line scan shown above is specific to the chemical signature of the VSAM and the decreasing magnitude in this signature indicates degradation after packaging and after stress at 300 C for 50 and 100 hours.

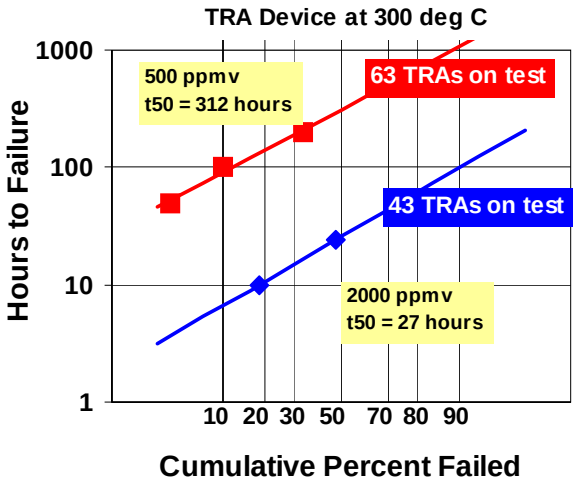


Figure 9. Failure data for a TRA device driving a load indicates a definite dependence on humidity.

*Failure Analysis of TRA devices*

Failures were identified in TRA devices held at 300°C for 10, 24, 50, 100 and 200 hrs. Failure analysis focused on regions where small gaps and contact areas are present. In the case of the TRA

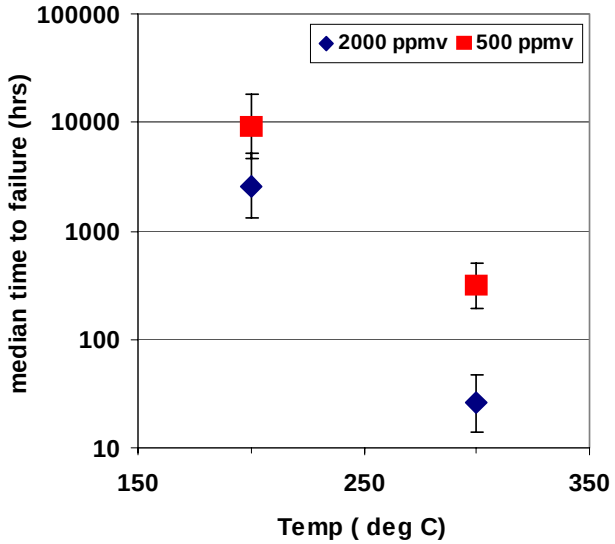


Figure 10. The median time to failures from all experiments is shown here. The error bars are statistical indications of 90% confidence intervals. The trend indicates longer life at lower temperatures and humidity levels.

device used in this experiment, contact is found between the anti-reverse pawls and the ring gear, ratchet pawls and the ring gear, guides and the ring gear, ring gear and the load gear, load gear and the hub, and finally the load gear and the toggle beam. These areas are shown in Figure 1. Several samples were tested using temperature as the accelerating factor. These devices were analyzed to determine the root cause of failure where failure is defined as the inability of the TRA to rotate the ring gear and hence load gear a single revolution.

Verifying the failure mechanism was critical towards determining which areas of the TRA device were responsible for failure. After verifying electrical continuity of the failed device(s), optical microscopy (of a stimulated device) was used to identify which component was likely the root cause of failure. Dynamic optical analysis revealed individual moving components thus eliminating them as potential locations of failure. Motion was observed along the actuator region with further analysis showing a slight movement in the ring gear. However, no motion was observed in the load gear. These results indicate the failure is not located at contact points in the anti-reverse pawls and the ring gear, ratchet pawls and the ring gear, guides and the ring gear, or the meshed teeth between the ring gear and the load gear. With this information, further analyses focused on the contact sites associated with the load gear and the toggle beam.

Scanning electron microscope (SEM) analysis of the toggle beam/load gear contact site revealed material bridging the two surfaces. Prior to testing, these devices were operated for ~ 60 cycles to establish functionality. Sixty cycles is well below the operational threshold to produce wear debris. As shown in Figures 11 a – c, foreign material is observed binding the toggle beam and load gear tooth. The binding material observed along the contact area in the failed samples was not observed in the contact area of a control device. Since the control sample was held in a dry nitrogen-filled box, it is likely this material was never present on the control sample.

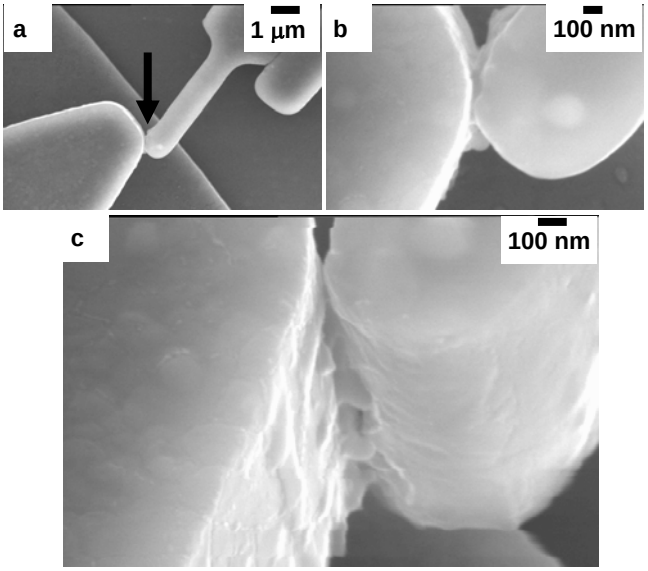


Figure 11 a, b, c. SEM micrographs reveal material bridging the toggle beam and the load gear tooth connecting them as a single, bridged component on a sample held at 300°C for 200 hrs.

Analysis of other contacting structures such as the ratchet pawl and ring gear, etc., did not reveal any binding material. It is possible the material existed but was obscured from view or the binding material possibly broke during the failure verification test.

The toggle beam and load gear contact area represents a region of the device that did not move during failure verification testing. Any material present in this area would not be damaged during failure verification. The small contact area and ease of accessibility made this region a logical choice for analysis but is likely not the root cause of failure. This is due to the size of the contact area (~ < 1 $\mu m^2$) compared to the force output (roughly 40 μN) of the TRA to the load gear. This binding material was observed in TRA devices failing at 300°C for 10, 24, 50, 100, and 200 hrs. This material was not observed for 100°C and 200°C samples tested at similar times. Due to the size and volume of the material binding the two components together, chemical analysis was not performed.

As mentioned previously, the size and location of the binding material would not provide sufficient force to stop the TRA from moving during normal operation, indicating it is not the root cause of failure. Partial removal of the hub region allowed successful movement of the TRA indicating that the presence of this binding material between the load gear and toggle beam contact region was not enough to prevent motion. Initial SEM analysis (not shown) did not reveal any foreign material on the hub. However, not all contacting areas are easily accessible via the SEM.

Using the focused ion beam (FIB), cross sections of the hub region were performed on aged samples and compared to a control. The FIB cross section control as shown in Figures 12, a and b, does not reveal any foreign material, contact or sticking sites on the hub and load gear. The FIB results for samples tested at 300°C for 200 hrs, 100 hrs, and 10 hrs revealed the presence of material adhering the gear to the hub. The location of this material varies from sample to sample, but the material is still observed between the gear and the hub region and may be located anywhere in the contact area around the 20 μm diameter hub. As shown in Figures 13, a, b, and c, the adhesion site can be located on the top, bottom, or sidewall surfaces of the gear and hub. The contact surfaces between the gear and the hub can potentially be much larger than the contact area of the toggle

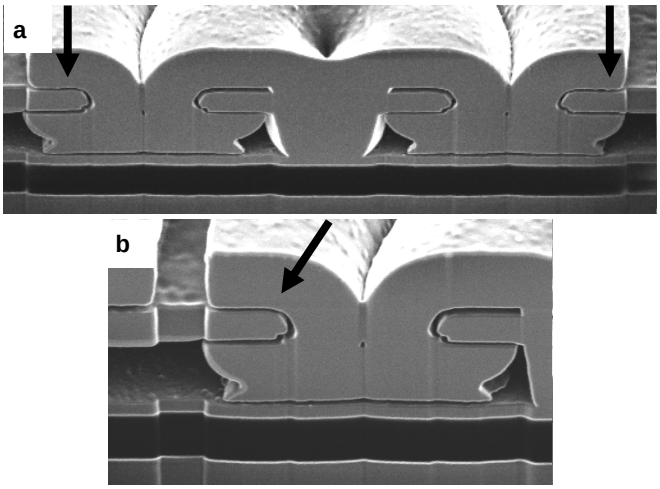


Figure 12. a) FIB cross section of a load gear hub. No adhesion or foreign material is observed along the gear to hub contact sites (arrows). b) close up of one side of the hub revealing the gap between the gear and the hub (arrow).

beam and load gear tooth. The hub/gear contact area may be large enough to prevent the TRA from moving the load gear. The binding sites observed are small and difficult to access for chemical analysis.

Further evaluation of the TRA functionality was performed by removing a load gear and operating just the TRA. Results from this experiment revealed the TRA functioned under normal operating conditions without the presence of the load gear. This result indicates that devices with large surface area contact risk failure due to binding more readily than devices without these large contacting surface areas. We believe this is the reason for TRA functionality without the load gear attached. This result also indicates that the TRA itself (without a load gear) is more robust to these accelerated lifetime test conditions than devices with large contacting areas or devices with numerous small gap spacing.

These findings bring into question the understanding of how the adhesion took place. It is possible the adhesion site has an accumulation of material locking the gear to the hub. We have shown in the earlier sections of this paper that the VSAM coating degraded significantly in these experiments. The adhesion in the hub may be due to cross-linking of the monolayers through silane linkages that were not saturated in the deposition process. It is also possible that oxidation at 300°C for extended periods of time displaced the monolayer and allowed oxide bridging to fuse the components together rendering the device inoperable. The polysilicon structures are of different crystallographic orientation, thus oxidizing at different rates. A third possibility is that no oxidation took place, but contact of the native oxide surfaces resulted in bonding across the interface (cold welding) at 300°C rendering the device inoperable. Further chemical analysis might reveal the root cause, however, the sites are extremely small making identification challenging.

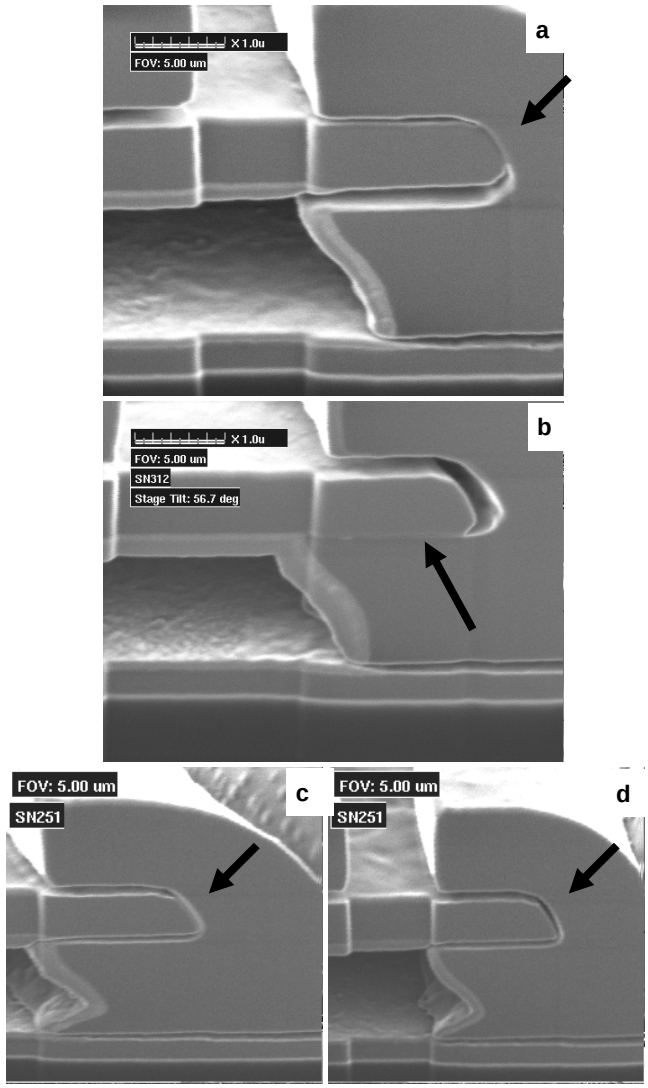


Figure 13. FIB cross sections revealing the binding sites of **a)** 300°C for 200 hrs, b) 300°C for 100 hrs, and c) 300°C for 10 hrs. All cross sections reveal an adhered region between the gear and the hub that would prevent motion given the force exerted by the TRA. d) After further FIB cuts into the region depicted in c the adhesion site has been completely removed.

## SUMMARY

All of our measurements reveal degradation of the VSAM surface coating when stressed at high temperatures with controlled humidity. In particular, we have seen the surface adhesion change for experiments stressed at 300°C for time intervals of 10, 24, 50, 100, and 200 hours. But there is no measurable change at 2 hours. A four times increase in humidity promotes the same change in a factor of ten less time.

The complex MEMS devices used followed the same trends as the test structures. We definitely observe a failure of the TRAs due to the environment with most failures occurring at 300°C and some failures at 200°C. These failures are due to an adhesion site in the hub of the load gear where the typical gap is 0.3 μm.

These experiments have defined the next steps to take. We plan to perform the same series of experiments at 250°C to compliment what we have done here. Additionally, we will perform experiments at 5000 ppmv to gain a better understanding of the humidity effect.

## CONCLUSIONS

We have determined that failures in complex MEMS devices can be accelerated using high temperatures and controlled humidity environments. The failures are dependent on both temperature and humidity. The trend indicates longer life at lower temperatures and humidity levels.

We have shown that the TRA failures relate to measurable changes in contacting surfaces using test structures and surface analysis techniques. Shorter time intervals at higher humidity produce the same surface degradation as longer times at lower humidity.

## ACKNOWLEDGEMENTS

We give special thanks to Scot Swanson for assembling an oven array and Frere McNamara for the chemical wash of the tubes. We also thank Rich Plass and Leslie Phinney for review and discussion. Sandia is a multi-program laboratory operated by Sandia Corporation, a Lockheed Martin Company, for the United States Department of Energy under contract DE-AC04-94AL85000.

## REFERENCES

[1] U. Srinivasan, M.R. Houston, R.T. Howe and R. Maboudian, "Alkyltrichlorisilane-Based Self-Assembled Monolayer Films for Stiction Reduction in Silicon Micromachines," *J. Microelectromechanical Systems* **7** (1998) pp. 252-260

[2] G.J. Kluth, M. Sander, M.M. Sung and R. Maboudian, "Study of the Desorption Mechanism of Alkylsiloxane Self-Assembled Monolayers Through Isotopic Labeling and High Resolution Electron Energy-Loss Spectroscopy Experiments," *J. Vacuum Sci. and Technol.* A16 (1998), pp. 932-936.

[3] M.T. Dugger, R.J. Hohlfelder and D.E. Peebles, "Degradation of Monolayer Lubricants for MEMS," *Proc. SPIE - The International Society for Optical Engineering*, 4980 (2003) pp. 138-150.

[4] M. G. Hankins, P. J. Resnick, P. J. Clews, T. M. Mayer, D. R. Wheeler, D. M. Tanner, and R. A. Plass, "Vapor deposition of amino-functionalized self-assembled monolayers on MEMS," *Proceedings of the SPIE - The International Society for Optical Engineering*, 2003; V4980, pp. 238-47.

[5] S. T. Patton, W. D. Cowan, K. C. Eapen, and J. S. Zabinski, "Effect of surface chemistry on the tribological performance of a MEMS electrostatic lateral output motor," *Tribology Letters*, 2001; V9, No. 3-4, pp. 199-209.

[6] H. W. Liu and B. Bhushan, "Adhesion and friction studies of microelectromechanical systems/nanoelectromechanical systems materials using a novel microtriboapparatus," *Journal of Vacuum Science & Technology*, 2003; V21, No.4, pp. 1528-1538.

[7] S. Barnes, S. Miller, S. Rodgers, and F. Bitsie, "Torsional Ratcheting Actuating System," *Inter. Conf. On Modeling and Simulation of Microsystems*, San Diego, CA, March 2000, pp. 273-276.

[8] D. M. Tanner, J. A. Walraven, S. S. Mani, and S. E. Swanson, "Pin-Joint Design Effect on the Reliability of a Polysilicon Microengine," *Proceedings of IRPS*, 2002, pp. 122-129.

[9] M. P. de Boer and T. A. Michalske, "Accurate method for determining adhesion of cantilever beams," in *Journal of Applied Physics,* V 86, No. 2, 15 July 1999, pp. 817-827.

[10] J. A. Ohlhausen, et al., "Multivariate statistical analysis of time-of-flight secondary ion mass spectrometry images using AXSIA," in *Applied Surface Science*. 231-232 (2004) p.230-234.

[11] W. Nelson, *Accelerated Testing: Statistical Models, Test Plans, and Data Analyses*, New York: John Wiley & Sons, 1990, ch. 3, pp. 145-154.